A 3D synthetic rock mass numerical method for characterizations of rock mass and excavation damage zone near tunnels

Yabing Zhang[1] · Xinrui Liu[2] · Tianhong Yang[1] · Peng Jia[1] · Xin Liu[3] · Fengyu Ren[1]

Abstract
In practice, a damage zone is generally formed after tunnel excavation in jointed rock mass. This damage zone is closely related to rock mass properties and requires careful examination in order for cost effective supporting designs. In this research, a synthetic rock mass (SRM) numerical method is applied for characterizations of the jointed rock mass and excavation damage zone (EDZ) near underground tunnels in 3D. The SRM model consists of bonded particles and simulates deformation and crack propagation of the rock mass through interactions between these particles. The effects of joint stiffness and distribution on the rock mass properties are systematically examined by comparing the numerical data with an empirical geological strength index (GSI) system and an associated Hoek-Brown strength criterion. The numerical results suggest that rock mass properties are comparable to the empirical GSI/Hoek-Brown system only when inclined joints are simulated in the rock mass subjected to axial loading. The rock mass is strengthened and the empirical GSI/Hoek-Brown characterization becomes inappropriate when the joints are less favorable to shear sliding. The SRM method is then applied for characterizations of tunnel EDZ. It appears that the depth and location of the EDZ are a function of the tunnel orientation, joints, and in situ stresses. The EDZ depth is expected to be higher when inclined joints are simulated. The EDZ area is reduced when the joints in the rock mass are horizontally and vertically distributed.

Keywords Synthetic rock mass · Excavation damage zone · GSI/Hoek-Brown system · Crack distribution

Introduction

Tunnel excavation is associated with damages in the surrounding rocks. The excavation activities alter the originally equilibrated state of the rock mass, introducing tensile and shear failures of discontinuities and intact rocks. This disturbance generally develops an excavation damage zone proximity to the tunnels, introducing irreversible deformation with crack formation and propagation (Perras et al. 2015; Gong et al. 2020). The depth of the EDZ is a key factor needs to be considered for tunnel supporting design. The EDZ characterization has largely relied on empirical methods (Martin and Christiansson 2009), or numerical methods (Yang et al. 2013; Zhang et al. 2016; Lei et al. 2017; Yang et al. 2019). These research works show significant progresses on this issue; however, some limitations still exist. The empirical methods may be case-specific and become inapplicable for other tunnel sites with different geological settings. The numerical methods may be based on either 2D assumption, or fail to explicitly include discontinuities in the models. Consequently, some inherent inaccuracies attributed to the model simplifications may be inevitable. The tunnel EDZ is predominantly controlled by the rock mass properties for a given environment of in situ stresses. Cost effective supporting to the tunnels depends on reliable knowledge of the rock mass, such as strength and deformability. Nevertheless, characterizing jointed rock mass at an adequate confidence level remains a challenging issue in rock mechanics and engineering community. The jointed rock mass behaves in reality as a mechanically heterogeneous and anisotropic material, due to the existence of discontinuities, such as faults, foliations, veins, and joints. The rock mass properties are controlled by both the discontinuities and stress-induced

✉ Xinrui Liu
 xliu1984@qq.com

1 Key Laboratory of Ministry of Education on Safe Mining of Deep Metal Mines, Northeastern University, Shenyang, China

2 Institute of Land Resource Management, Northeastern University, Shenyang, China

3 Shenyang Geotechnical Investigation & Surveying Research Institute, Shenyang, China

cracks formed in the rock bridges. The discontinuities prevent development of rigorous mathematical solution for the calculation of the rock mass properties. The reliability of the field testing data may be questionable due to the scattering nature. A reliable method is requested for characterizations of both the rock mass and the tunnel EDZ.

The synthetic rock mass approach is a 3D numerical tool developed for characterizing rock mass properties (Mas Ivars et al. 2011). The fundamental element in the SRM model is particles, and the mechanical behavior of the rock mass, such as cracking and deformation, is simulated by detecting relative movements between these particles. The particles are tightly assembled and bonded, and a crack is marked when the stress developed between the two particles destroys the assigned bond. Due to its discrete configuration, the SRM can simulate rock mass discontinuities in an explicit manner, by assigning different strength and stiffness parameters at the particle contacts along the path of each discontinuity in the model. The SRM calculates the rock mechanical behavior by focusing on the particle interactions, requiring no macroscopic constitutive parameters of the rock mass, such as cohesion or friction angle. Instead, these parameters are its numerical products. This method can be selected as a new technique for rock mass characterization, and further, the EDZ evaluation for underground tunnels in 3D environments. To date, the SRM database for modeling jointed rock masses at the engineering scale is still limited. Researchers may distrust this method and would rather use simple continuum models based on the widely used GSI/Hoek-Brown system (Hoek et al. 2013). The GSI/Hoek-Brown characterization is developed progressively over years of engineering practice, and is routinely used for either direct rock mass characterization or selected as theoretical basis of numerical models among rock engineering designers. A comparison study between the numerical and empirical methods will testify the robustness of the SRM model and provide a new numerical tool for the characterization of the tunnel EDZ in various geological configurations.

In this paper, the SRM approach is initially verified by the empirical GSI/Hoek-Brown system, through uniaxial and triaxial compressive tests. The effects of stiffness and orientation of discontinuities on the model strength and deformability are investigated. Additional SRM tunnel models are constructed, and the simulated excavation damage zones around tunnels are thoroughly characterized.

The SRM model and GSI/Hoek-Brown characterization system

The SRM model uses a discrete element code, PFC3D (Itasca 2012). It is essentially built by explicitly incorporating rock mass discontinuities in a particle assembly. Particles in the assembly are assumed to be 3D rigid spheres allowing overlap

in between. Therefore by assigning stiffness to these particles, internal forces are formed in normal and shear directions in case relative particle movements occur. To simulate intact rocks in the mass, the particles are tightly packed and conceptually bonded. A crack at the particle scale is marked when the forces corresponding to a particle pair exceed the nominal bond strengths. More cracks emerge and gradually coalesce to form one or multiple macroscopic fractures when external loading is applied to the model. These macroscopic fractures eventually coalesce with initial discontinuities to form global failure channels of the rock mass, generally behaving as splitting or shearing types. The particle stiffness, friction, and bond strength are calibrated on the basis of laboratory data. The strength, deformation modulus, and Poisson's ratio of intact rocks monitored from laboratory tests are used to constrain the particle parameters. Robustness of this bonded particle model has been verified by comparing numerical models with laboratory tests on rock samples, such as the research works conducted by Zhang and Wong 2012; Bahrani and Kaiser 2016.

The SRM model is then constructed by incorporating discontinuities in the particle assembly. Discontinuities are realized as a form of discrete fracture network (DFN), relevant parameters including orientation, intensity, and size (Rogers et al. 2015). In this research, the "joint" and "fracture" are synonyms to discontinuities of the rock mass. Each discontinuity is explicitly simulated by assigning different mechanical parameters to the particle contacts where it is passing through. A smooth joint logic is used to overcome unrealistic bumpiness along each discontinuity, resulting from the spherical particle assumption. This logic neglects particle shape and allows smooth sliding (Itasca 2012). The robustness of the smooth joint has also been validated by comparing the sample scale SRM models with laboratory tests. For instance, Bahaaddini et al. 2013 conducted validation study for the SRM models by simulating similar failure modes of rock samples observed in laboratory tests. Vallejos et al. 2016 used the SRM method to model veined core-size samples, and confirmed the capabilities of this numerical model to re-produce the behavior of veined rock samples under uniaxial loading conditions.

The 3D configuration of the SRM model uses no plane stress or strain assumptions, providing more reliable numerical results for jointed rocks. The model focuses on interactions at the particles scale, requiring no macroscopic constitutive parameters. It distinguishes intact rocks and joints in the rock mass, and explicitly simulates crack propagations in the intact rocks in a realistic manner. These advantages make the SRM method a powerful tool for analysis of rock mechanics-related problems. More details of the SRM model are introduced in references by Zhang et al. (2015) and Mehranpour et al. (2018).

The GSI/Hoek-Brown system has been routinely applied for rock engineering projects (Hoek et al. 2013; Marinos

2019; Song et al. 2020). It is widely used for characterizing rock mass by field observations on structures of the rock matrix and joint surface quality. The structure is rated from intact/massive to blocky and laminated/sheared, while the surface quality is rated from very good to fair and very poor. In this configuration, a high GSI value corresponds to a rock mass with few rough discontinuities. The GSI is best suited to moderately jointed rock mass, and may become inappropriate for massive rocks or heavily fractured rock mass. Its application requires extensive field experience, and subjectivities may arise during this process. To overcome this, Cai et al. (2004) proposed a rock block volume (V_b) to replace descriptive rating of rock mass structure. In this paper, the rock block volume is used for GSI quantification. For a DFN model representing the rock mass structure, the average block volume is quantified by a parameter of volumetric joint count (J_V). This parameter is a 3D representation of the joint intensity, numerically equal to the discontinuity number cutting a unit cube, following Eq. 1 (Palmstrom 2005). In this research, J_V is derived by averaging traces on nine cubes placed in the discrete fracture networks. After the GSI quantification, the Hoek-Brown criterion is applied to calculate rock mass strengths, following Eqs. 2–5.

$$V_b = \beta \times J_V^{-3} \qquad (1)$$

where β is the block shape factor, and its value is suggested to be 36.

$$\sigma_1 = \sigma_3 + \sigma_{ci}\left(m_b\frac{\sigma_3}{\sigma_{ci}} + s\right)^a \qquad (2)$$

$$m_b = m_i\exp\left(\frac{GSI-100}{28-14D}\right) \qquad (3)$$

$$s = \exp\left(\frac{GSI-100}{9-3D}\right) \qquad (4)$$

$$a = \frac{1}{2} + \frac{1}{6}\left(e^{-GSI/15} - e^{-20/3}\right) \qquad (5)$$

where σ_1 and σ_3 are the maximum and minimum effective stresses; m_i depends on mineral constituent and can be approximated as the ratio of compressive/tensile strengths of the laboratory sample; D is a blasting disturbance factor; σ_{ci} is the laboratory rock strength of uniaxial compression. The GSI and D are also applied for quantifying the modulus of the rock mass (E_m) on the basis of laboratory sample modulus (E_i), following Eq. 6 (Hoek and Diederichs 2006).

$$E_m = E_i\left(0.02 + \frac{1-D}{1 + \exp((60 + 15D - GSI)/11)}\right) \qquad (6)$$

Rock mass characterization using the SRM method

DFN realization and correlation to the GSI system

The advantages of the SRM model, including its 3D configuration, free of constitutive parameters, and explicit simulation of discontinuities and crack propagation, make it a powerful tool for rock mass characterization. If the mechanical parameters derived from the SRM models match the GSI/Hoek-Brown parameters based on years of engineering experiences, this method can then be reliably used for characterizing the tunnel EDZ and providing designing references. The first key aspect linking the SRM model to the GSI/Hoek-Brown system is to rate rock mass structure from a given DFN, through the average volume of rock blocks. Considering that three joint sets intersecting each other with large angles are commonly observed in practice, the DFN realized in this paper consists of three joint sets. The dips of joint sets A and B are defined as 60°, and the dip directions are defined as 0° and 90°, respectively. The dip and dip direction of the third joint set C are defined as 39° and 225°. The joint intensity is denoted by the total area of joints per unit volume. This parameter is $1.5 m^2/m^3$ in this paper, representing moderately jointed rock mass. The DFN is generated in a 3D space of 10.0 m and 10.0 m in width and height, and the fractures outside the rock mass volume, with its width and height defined as 3.0 m and 6.0 m, are truncated to remove boundary effects (Fig. 1a).

An additional DFN model is generated by rotating the three joint sets to further characterize the rock mass when the joint orientations are altered. The DFN consists of horizontal and vertical joint sets (Fig. 1b). The volumetric joint count J_V is tracked and averaged by traces between the joints and unit cubes (Fig. 1c–d). The J_V of the initial DFN model is averaged as 6.11, implying that more than 6 joints intersecting a random cubical space. The rock block size (V_b) is estimated using Eq. 1, as $0.16 m^3$. The J_V of the following DFN is 5.85, and the corresponding rock block volumes is $0.18 m^3$. It appears that the rotation of the joint sets only slightly changes the rock block volume, resulting in limited effects on GSI quantification. The second key aspect of relating the SRM model to the GSI system is to assign appropriate mechanical parameters to the joints in the SRM model, in order to match the surface quality described in the GSI chart. To date, no widely accepted relationship exists regarding this issue. A friction angle of 26° without cohesion and tension is suggested to match the "FAIR" surface quality (Poulson et al. 2015). In this research, the joints in the DFN models are assigned a friction coefficient as 0.5 (friction angle 26.6°), and the GSI of the two DFN models is quantified as 55 by integrating the rock mass structure and surface quality (Cai et al. 2004).
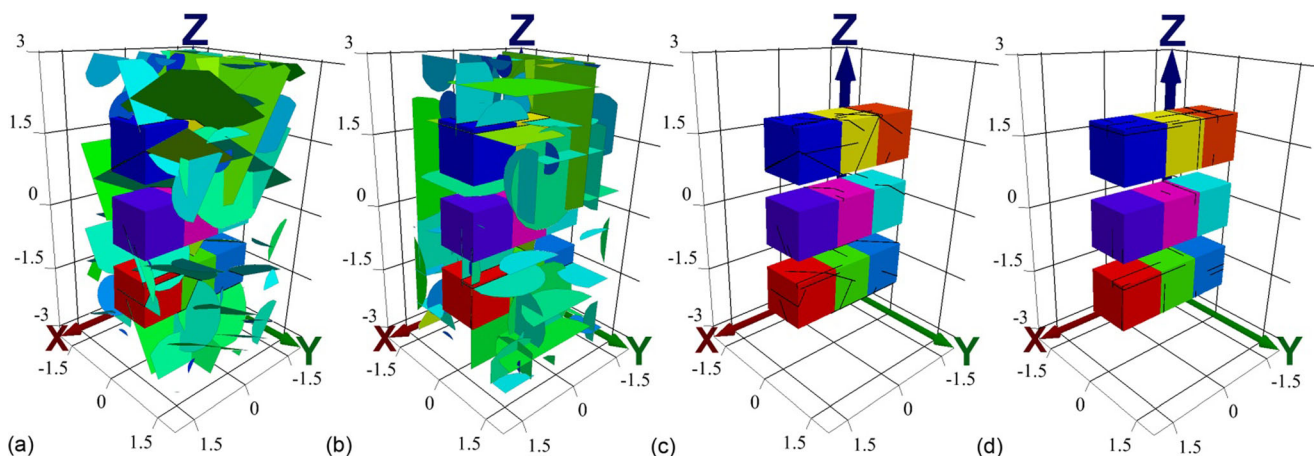
Fig. 1 Calculation of rock block volume: **a**, **b** are DFN models; **c**, **d** are traces between joints and cubes. The volumetric joint count of J_V is averaged as 6.11 and 5.85; the rock block volume is calculated as 0.16m^3 and 0.18m^3. Model scale: meter

SRM model calibration and comparisons with the GSI/Hoek-Brown system

The assignment of SRM parameters differs from conventional continuum models. The SRM distinguishes intact rocks and discontinuities; therefore, the parameters assigned to intact rocks differ from the parameters assigned to discontinuities. In this paper, the intact rock consists of a bonded particle assembly. The width and height of the assembly are defined as 3.0 m and 6.0 m, same as the volume selected for DFN analysis. Particle size is determined to balance accuracy and simulation time. In this paper, the particle size is defined between 4.0 and 8.0 cm. The particle parameters, including stiffness and bond strengths in normal and shear directions, and friction angle between the particles, are calibrated and listed in Table 1. Mechanical parameters used for calibration are derived from laboratory tests on sandstone, including uniaxial compressive strength (140.0 MPa), modulus (30.0 GPa), and Poisson's ratio (0.25). Specifically, a set of parameters is

assigned, and the particle assembly is subjected to uniaxial compression until failure; the macroscopic properties of the assembly are monitored and compared with the target properties of the sandstone. The set of particle parameters is calibrated until the numerical results are consistent with the target rock properties. This modeling configuration is clearly different from the continuum models, where the macroscopic mechanical properties are assigned directly to the model elements, requiring no calibration. The particle model essentially follows the principle as laboratory physical tests, except in a numerical manner. It requires no macroscopic constitutive parameters, and by explicitly simulating discontinuities in the model, the SRM method has the ability to characterize the rock mass parameters via numerical uniaxial and triaxial tests on the models.

Two SRM models are built by simulating the DFNs in the particle assembly. The model width and height are defined as 3.0 m and 6.0 m, identical to the volume used for DFN realization. The volume is ideally exceeding the representative element volume, which is defined as the minimum volume of the rock mass showing unchanged mechanical properties. This volume depends predominantly on joint rock mass structure, and can be derived by the SRM method. The model size used in this research is similar to the geometrical representative element volume proposed by Esmaieli et al. (2010). The SRM models appear similar to the DFN models, except that the voids between joints are filled with bonded particles. For description convenience, the two SRM models are marked as G60 and G90, corresponding to the joint set dips of 60° and 90°, respectively. The friction coefficient of 0.5 with zero cohesion and tension of joints is suggested corresponding to the "FAIR" joint description, and is used for the SRM models. After this, the joint stiffness becomes the remaining parameter requiring calibration. In this research, the stiffness is assumed equal in the normal and shear directions, and increased from 10.0 to 20.0, 50.0, and 100.0 GPa/m. The SRM models are

Table 1 Calibrated parameters for the bonded particle assembly

Definition	Values
Particle	
Size (cm)	4.0–8.0
Density (kg/m^3)	2500.0
Stiffness in normal (GPa/m)	27.0
Stiffness in shear (GPa/m)	13.5
Friction angle (°)	45.0
Particle bond	
Stiffness in normal (GPa/m)	27.0
Stiffness in shear (GPa/m)	13.5
Bond strength in normal (MPa)	25.0
Bond strength in shear (MPa)	25.0

then subjected to uniaxial loading in the vertical Z direction. The axial stress-strain relationships of the G60 models are plotted in Fig. 2a. The corresponding peak strength and modulus are shown in Table 2. The strength is obviously influenced by the assigned joint stiffness, increasing from 29.4 to 34.5 MPa. The modulus meanwhile increases from 10.1 to 13.1 GPa. The reason is that normal stress occurring on each joint increases with the assigned stiffness at a prescribed axial strain level. This eventually leads to a higher level of shear strength of each joint and the global rock mass strength. Meanwhile, softer joints are responsible for the lower modulus derived from the SRM rock mass models, explaining the positive relation between joint stiffness and rock mass modulus.

A relationship is then built between the SRM models and the GSI/Hoek-Brown system. The GSI quantified from the DFNs is 55, so that the Hoek-Brown strength and modulus are calculated as 32.9 MPa and 12.2 GPa, respectively. Note here the parameters of m_i and D in Eq. 3, which are related to the rock mineral composition and blast disturbance to the rock mass, respectively, are defined as 15 and 0. Note also that the Hoek-Brown strength presented denotes the rock mass

Fig. 2 Axial stress-strain monitored from the uniaxial models of G60 and G90: **a** G60; **b** G90

strength in uniaxial compressive condition. The strength is not directly calculated using Eq. 2, but is linearly fitted to follow a Mohr-Coulomb strength criterion. The SRM strength and modulus are suggested to match the GSI/Hoek-Brown parameters when the joint stiffness is 50.0 GPa/m. For the G90 models, the SRM peak strength and modulus agree no more with the GSI/Hoek-Brown parameters, as shown in Fig. 2b and Table 2. The peak strength increases from 70.3 to 95.4 MPa, and the modulus from 21.4 to 31.8 GPa. These parameters are much higher than the corresponding GSI/Hoek-Brown parameters, suggesting that the GSI/Hoek-Brown system may underestimate the rock mass properties where the simulated joints are less favorable to shear sliding along them. In that condition, the rock mass failure is controlled predominantly by the failures of intact rocks. The intact rocks are much stronger than joints, leading to higher strength and modulus of the rock mass. The merit of the SRM method lies in the circumstances where the empirical GSI/Hoek-Brown system becomes less appropriate for the target rock mass characterization.

Cracking characteristics in the rock mass are also investigated, serving as the secondary dataset to demonstrate the failure mechanisms. Figure 3a shows 3D crack distribution of the G60 model when the stiffness of joints is 50.0 GPa/m. In order for clear views, localized models are derived by clipping the cracking model in two thin layers. A long fracture is simulated in the center of the model, initiating from the top inclined joints and linking the lower joints. Figure 3b shows that the model is split and dilates in the X direction. Figure 3c shows the localized layer parallel to the splitting fracture, where the failed rocks are concentrated in the middle. Figure 3d shows the global cracking model simulated in the G90 model. In uniaxial compressive loading, the horizontal and vertical joints still play an import role of serving as weak planes and stress concentration sources, albeit the shear failure of joints is less prone to occur due to the joint orientation. Figure 3e shows a similar splitting fracture as observed in the G60 model. Figure 3f shows failed rock blocks in the layer parallel to the Y direction.

Triaxial compression models (marked as T60) are further conducted for one of the G60 models with joint stiffness being 50.0 GPa/m, where the peak strength and modulus coincide with the GSI/Hoek-Brown parameters. The uniaxial strengths based on the SRM and GSI/Hoek-Brown system are 33.1 MPa and 32.9 MPa, for references. The axial stress-strain relationships are plotted in Fig. 4a. The parameters of strength and modulus are presented in Table 3. As expected, the rock mass is strengthened when confining stresses are applied. The peak strength increases from 33.1 to 48.3 MPa until 78.5 MPa when the confining stress is from 0.0 to 3.0 MPa until 12.0 MPa. These parameters agree in general with the GSI/Hoek-Brown strengths, as verified in Fig. 4b. Note again that the uniaxial strength derived from the GSI/
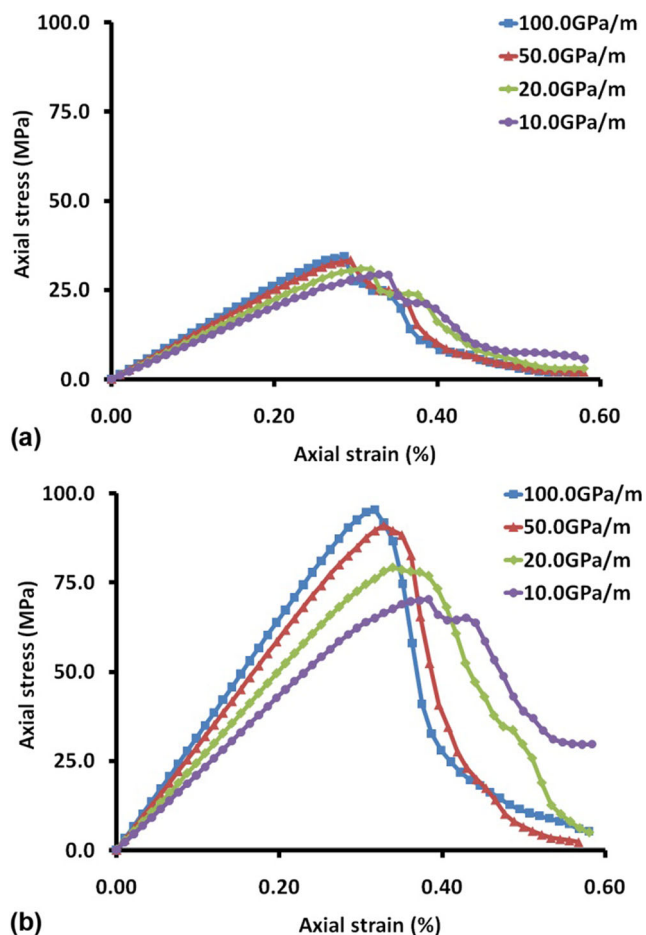
Table 2 Parameters of the uniaxial models with varied joint orientation and stiffness

Model group	Joint stiffness (GPa/m)	Peak strength (MPa)	Modulus (GPa)
G60	100.0	34.5	13.1
	50.0	33.1	12.4
	20.0	31.0	11.2
	10.0	29.4	10.1
G90	100.0	95.4	31.8
	50.0	91.0	28.9
	20.0	79.1	24.6
	10.0	70.3	21.4

The strength and modulus are empirically calculated as 32.9 MPa and 12.2 GPa when the GSI is 55

Hoek-Brown system, as 32.9 MPa, is calculated by fitting the Hoek-Brown equation using the Mohr-Coulomb criterion.

The agreement between the numerical and empirical methods testifies the robustness of the SRM approach, making it a
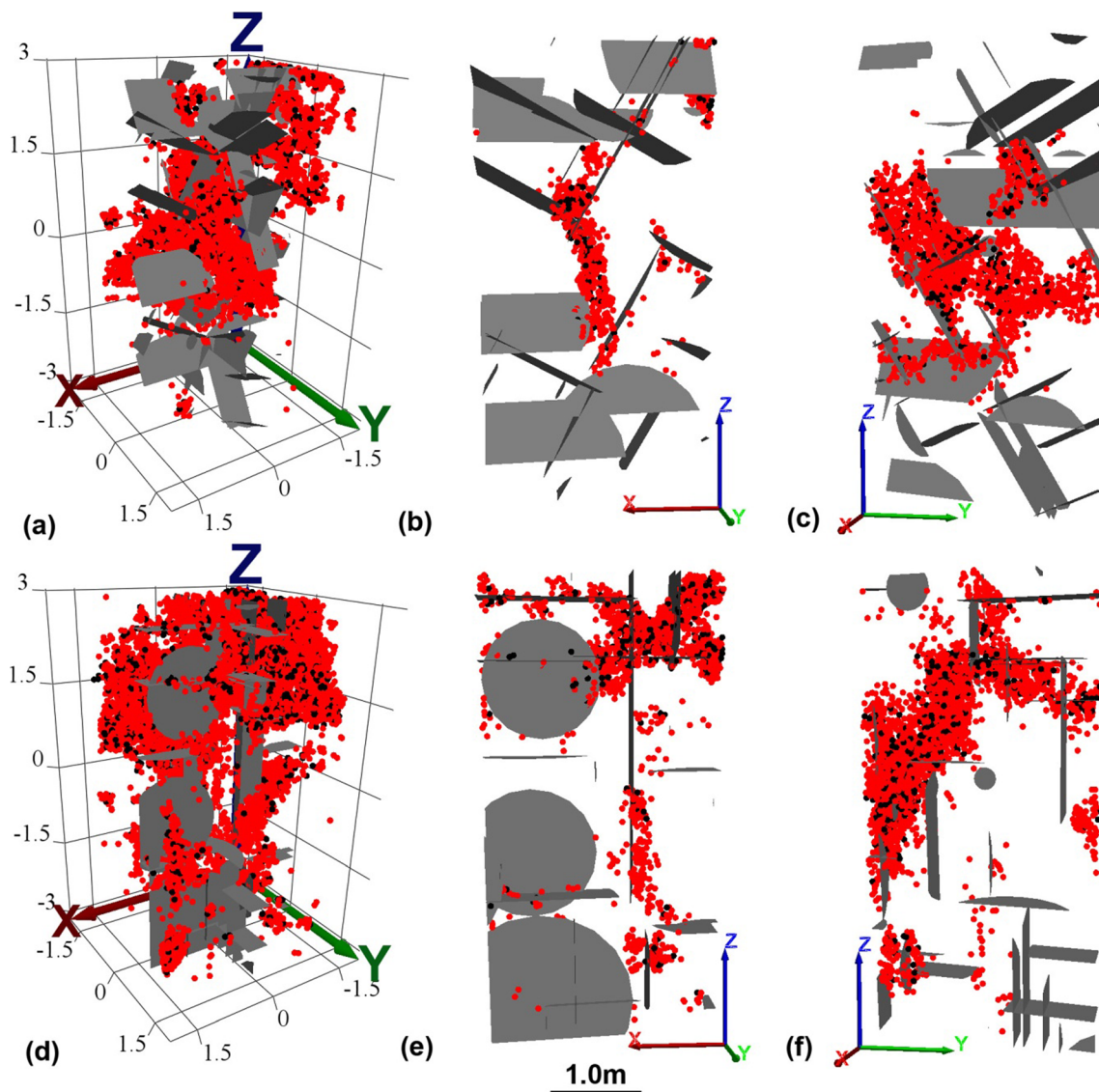

Fig. 3 Global and localized cracks simulated in the uniaxial models with joint stiffness of 50.0 GPa/m: **a–c** G60; **d–f** G90. The disks and dots denote initial joints and secondary cracks when the SRM models are subjected to external loading
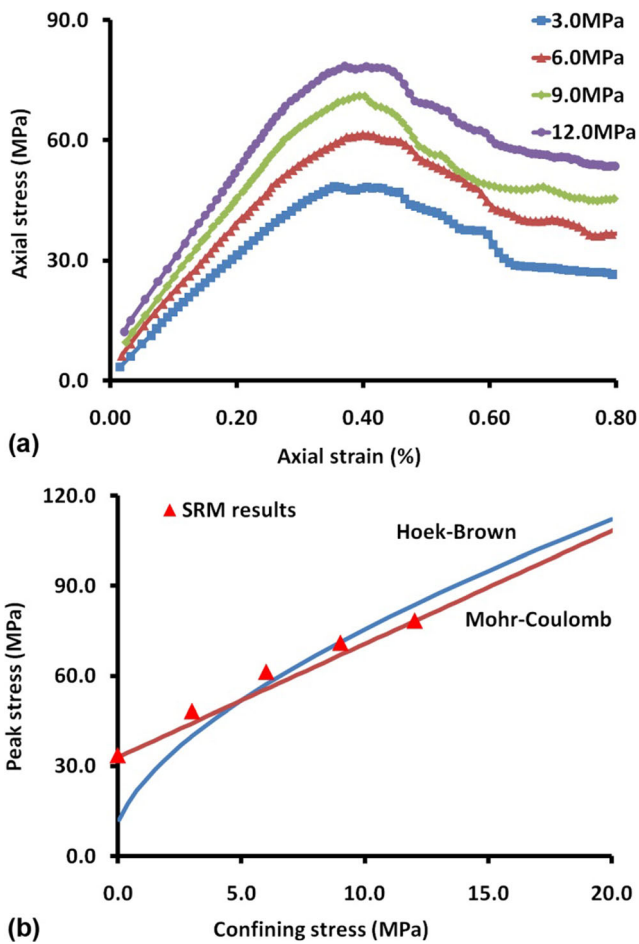
(a)

(b)

Fig. 4 Triaxial models of T60: **a** stress-strain relationships; **b** the SRM strengths and the strength criteria of Mohr-Coulomb and Hoek-Brown

direction when the confining stress is 3.0 MPa, as shown in Fig. 5a–c. The predominant failure mode of the rock mass remains unchanged when the confining stress is 9.0 MPa, with more cracks formed along the global shear zone, as shown in Fig. 5d–f. The changed failure mode implies the complexities of the rock mass failure in various loading conditions. While this kind of information is missing in the empirical GSI/Hoek-Brown system, the crack propagation in the rock mass is realistically simulated and captured by the SRM method. Corresponding mechanical parameters derived from this kind of simulations are therefore suggested to be reliable for rock mass characterization purposes.

Tunnel EDZ characterization using the SRM method

Model configuration

Characterizing tunnel EDZ is a challenging issue as the damage zone at the tunnel periphery depends predominantly on the relative orientations of the tunnel axis, rock mass discontinuities, and in situ stresses (Wang et al. 2017a, b). It is essential to investigate the interactions between these three factors, in order to propose cost effective-supporting designs. While the tunnel EDZ may be characterized using 2D models when the discontinuity strike is parallel to the tunnel axis, more accurate simulations are expected using the sophisticated SRM models, where the tunnel, discontinuities, and in situ stresses are all simulated in 3D (Wang et al. 2019). For this purpose, a cubical rock mass SRM model is constructed, with the length, width, and height defined as 10.0 m (Fig. 6a). The DFN inserted is similar to the DFN used for the previous G60 models, except that it is realized in a larger domain. Measurement sphere is used in SRM models to detect global and localized developments of stress and strain of the rock mass, depending on the sphere size. The stresses within the sphere are calculated by tracking the contact forces between particles, and the strains are tracked on the basis of a least-squares procedure (Itasca 2012). A sphere is placed in the center of the rock mass to detect the global mechanical behavior (Fig. 6b). Four smaller spheres are installed at the

reliable tool for characterizing jointed rock mass. Numerical results also suggest the increase in the rock mass modulus, from 12.4 to 16.7 GPa until 28.6 GPa. While the modulus characterization is missing in triaxial conditions when using the GSI/Hoek-Brown system, this parameter can be derived by the SRM method.

Cracking models are investigated in the triaxial models with the confining stresses of 3.0 MPa and 9.0 MPa. In comparison with G60, the axial splitting fracture in the middle of the model disappears. Instead, a global shear zone consisting of failed rock bridges and initial joints is simulated along the *Y*

Table 3 Parameters of the triaxial models with varied confining stresses

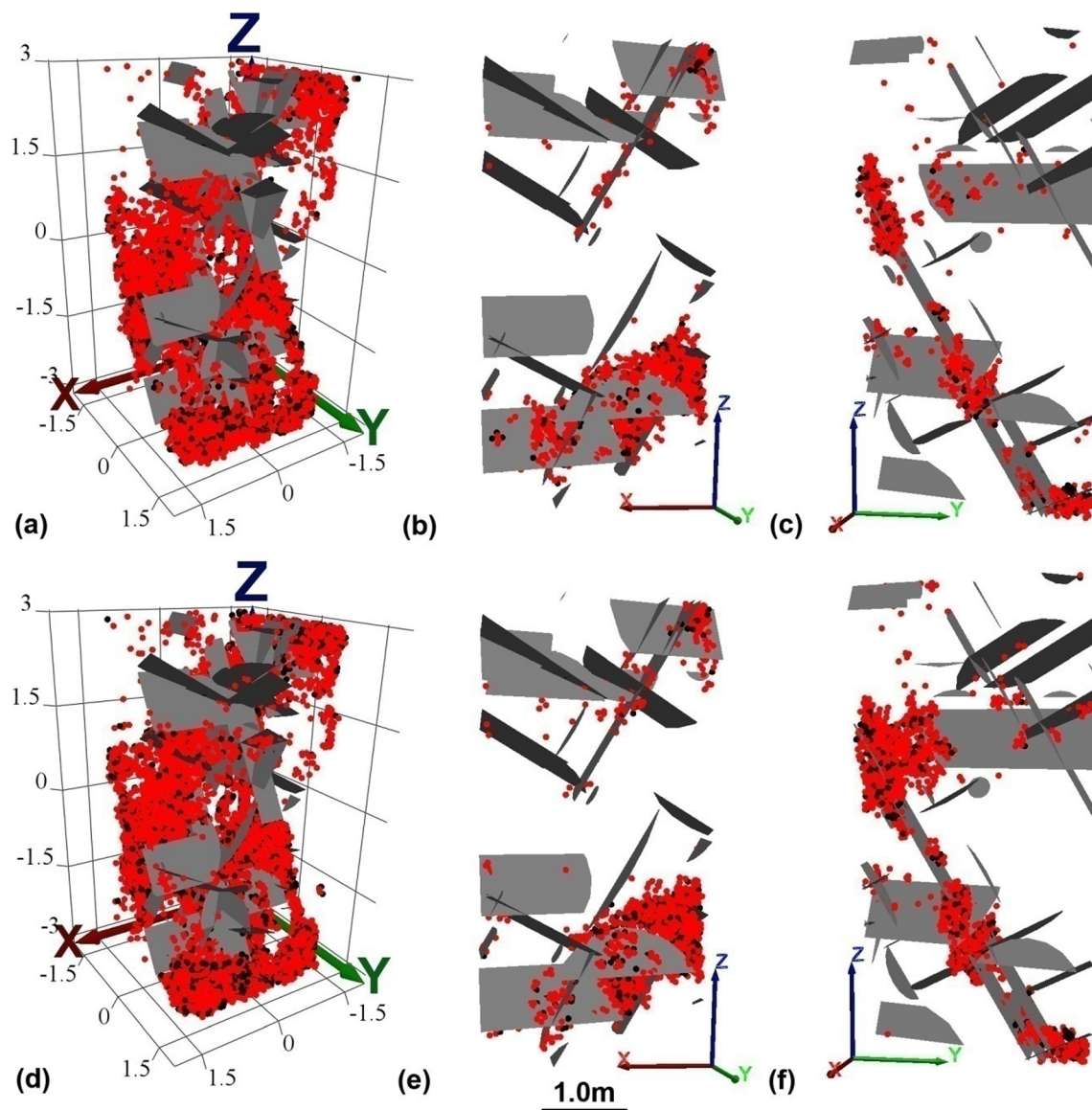| Model group	Confining stress (MPa)	Empirical Hoek-Brown strength (MPa)	SRM peak strength (MPa)	SRM modulus (GPa)
T60	3.0	39.9	48.3	16.7
	6.0	57.1	61.4	21.6
	9.0	71.2	71.1	25.2
	12.0	83.6	78.5	28.6
Uniaxial	0.0	32.9	33.1	12.4

Fig. 5 Global and localized cracks simulated in the triaxial models with joint stiffness of 50.0 GPa/m: **a–c** the confining stresses are 3.0 MPa; **d–f** the confining stresses are 9.0 MPa. The disks and dots denote initial joints and secondary cracks when the SRM models are subjected to external loading

boundaries of the tunnel to detect localized mechanical behavior (Fig. 6c). The tunnel is excavated in the middle of the rock mass, with a square cross section of 2.0 m, and a length of 4.0 m (Fig. 6c–d). This square profile is commonly used for deep mining tunnels, or more precisely, mining drifts. The tunnel axis is defined in the Y direction, and then changed to the X direction, so that the interactions between the tunnel orientation and the rock mass discontinuities are characterized. The rock mass is initially loaded in the three directions until the corresponding stresses reach the target values, in this paper as 10.0 MPa. As the initial stresses may be insufficient for the formation of the tunnel EDZ, the rock mass after excavation is subjected to continuous loading in one designated direction until EDZ occurs. In this manner, the tunnel EDZ

will be characterized in various combinations of the in situ stresses.

Effects of tunnel orientation and loading directions on the tunnel EDZ

Figure 7a shows the EDZ of the tunnel in the Y direction when the rock mass is predominantly loaded along the X direction ($\sigma_x = 75.0$ MPa). Note that at this initial stage of research, only the cross section of the tunnel is characterized. Typical notch failures are simulated near the tunnel roof and floor. The maximum stress is expected to be along the X direction; therefore, the tunnel EDZ is mainly generated in these locations, where the rock mass is severely squeezed

Fig. 6 Tunnel models for EDZ characterization: **a** jointed rock mass; **b** global measurement sphere; **c** localized measurement spheres (1–4) and transverse view of the tunnel; **d** longitudinal view of the tunnel
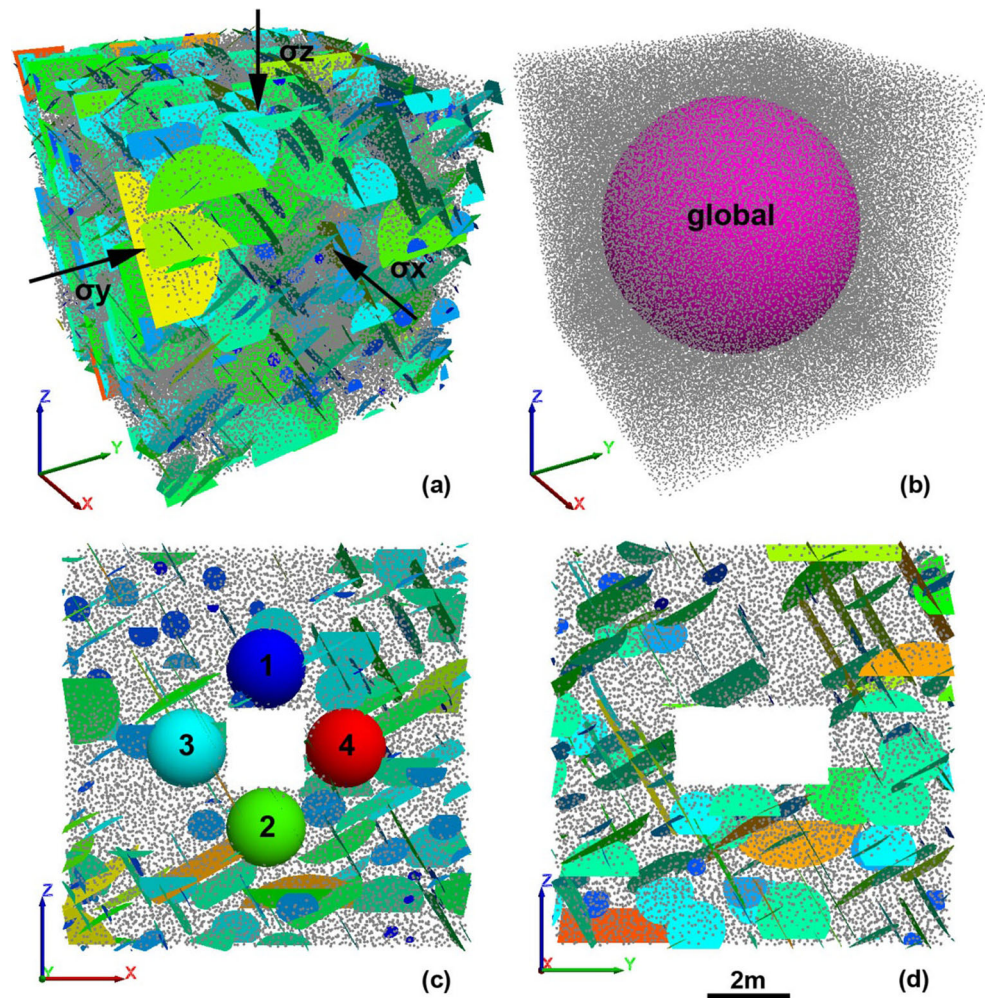
and stress concentration occurs. In contrast, no obvious damages are observed on the tunnel side walls. In this condition, the stability of the tunnel roof and floor is the key for supporting design. The damage zones are asymmetrically distributed, most likely due to the heterogeneous distribution of the initial joints. The depth of the EDZ is roughly measured as 1.0 r and 1.5 r near the tunnel roof and floor, respectively, where r is the radius of the circular tunnel and is approximated by the half length of the current tunnel (1.0 m). The EDZ depth is comparable to the empirical relationships (Eqs. 7–8) on the basis of case studies in various geo-environments (Martin and Christiansson 2009). The EDZ depth is empirically calculated as 1.0 r ($\sigma_{\theta\theta} = 215.0$ MPa; $\sigma_{sm} = 70.0$ MPa; $\sigma_{max} = 75.0$ MPa; $\sigma_{min} = 10.0$ MPa). The EDZ depth at the roof converges well between the numerical and empirical models. However, the numerical depth is deeper on the floor. While the empirical relationships provide general references to evaluate the tunnel EDZ depth, the SRM method is more accurate as it realistically simulates the mechanical interactions between the tunnel orientation, discontinuities, and in situ stresses in a 3D space.

$$S_d = r\left(0.5\frac{\sigma_{\theta\theta}}{\sigma_{sm}} - 0.52\right) \tag{7}$$

$$\sigma_{\theta\theta} = 3\sigma_1 - \sigma_3 \tag{8}$$

where S_d is the EDZ depth measured from the tunnel boundary; $\sigma_{\theta\theta}$ is the stress in the tunnel tangential direction; σ_1 and σ_3 are the maximum and minimum effective stresses; σ_{sm} is the spalling strength of the rock mass suggested to be 40–60% of the strength of the laboratory samples in uniaxial compression (140.0 MPa).

The tunnel EDZ can change significantly when in situ stresses are rotated. Figure 7b shows the EDZ distribution of the same tunnel model, except that the model is predominantly loaded in the Z direction ($\sigma_z = 75.0$ MPa). The rotation of the in situ stresses clearly alters the damage zone around the tunnel. No V-shaped notch failures are observed. Instead, the damage zones are formed symmetrically on the side walls, and extend along with the two major joint sets with the dip of 60°. The ultimate area of the EDZ is no longer limited to the

Fig. 7 Localized tunnel EDZ models: **a** tunnel in the Y direction, $\sigma_x = 75.0$ MPa; **b** tunnel in the Y direction, $\sigma_z = 75.0$ MPa; **c** tunnel in the X direction, $\sigma_x = 75.0$ MPa; **d** tunnel in the X direction, $\sigma_z = 75.0$ MPa. The confining stresses are 10.0 MPa in each model. The dips of the joint sets in the models are 60° and 39°. The disks and dots denote initial joints and secondary cracks when the SRM models are subjected to external loading
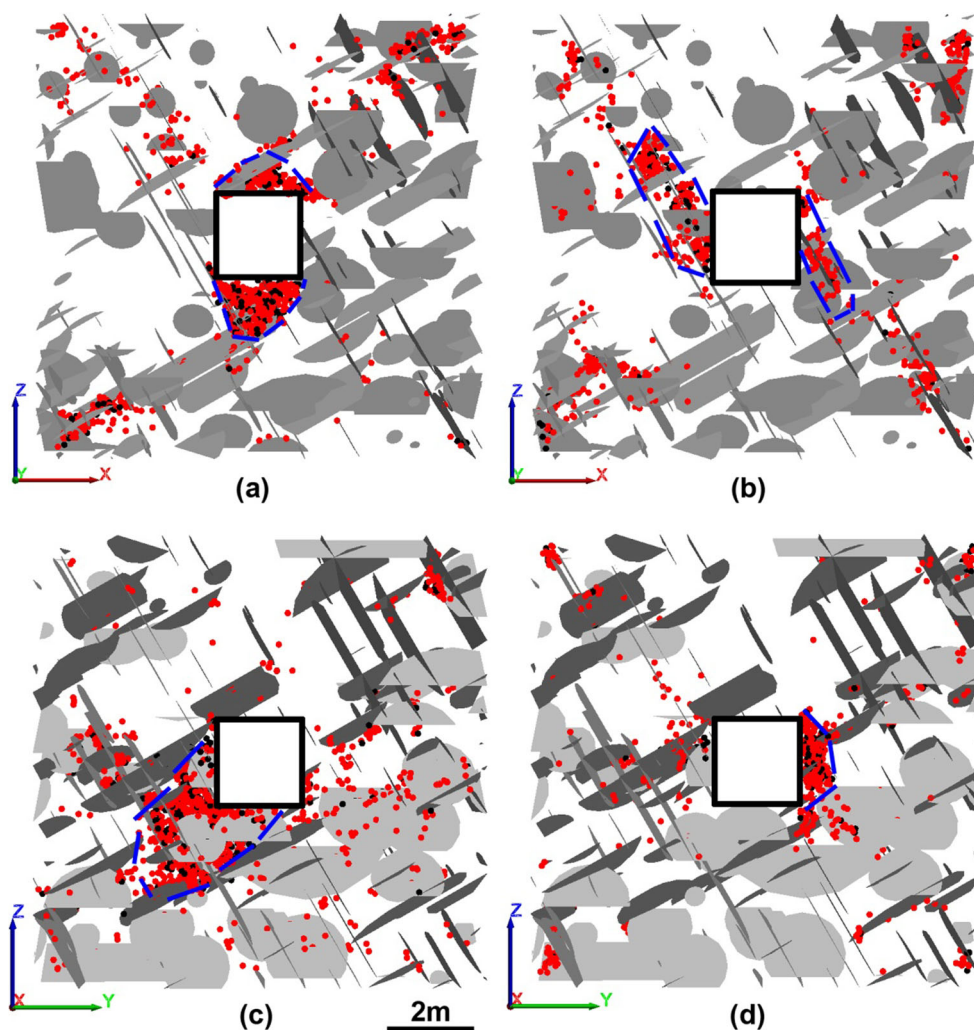
range of the side walls. The joint orientation favors EDZ formation when the model is squeezed in the vertical direction. As previously proved, the rock mass strength is significantly reduced with this combination of joints and in situ stresses, and the damage zone is prone to be formed in this manner. The EDZ depth of this model is suggested to be between 1.0 and 1.5 r. The EDZ distribution is further complicated when the tunnel is in the X direction, and loaded in the same X direction ($\sigma_x = 75.0$ MPa), as shown in Fig. 7c. The damage zone is mainly localized near the corner of the left side wall and floor. The rock mass within the damage zone is completely fragmented, leading to a maximum EDZ depth higher than 3.0 r (from the boundary of the EDZ to the tunnel corner). This suggests that the EDZ shape for a given combination of the tunnel orientation, discontinuities and in situ stresses may not always be the V-shaped notch failure. Figure 7d shows the same model as shown in Fig. 7c, except that the model is loaded in the Z direction ($\sigma_z = 75.0$ MPa). The EDZ is mainly localized near the right side wall, where the stress is concentrated. The EDZ depth is roughly measured as 1.0 r.

Interestingly no obvious damages are observed near the left side wall. Possibly more joints are distributed in that area and the stresses are lower due to the rock mass integrity. The tunnel failure may be structure controlled. In summary, the formation of the tunnel EDZ is controlled by a series of factors; therefore, the distribution of the tunnel EDZ is variable. No strict criterion exists to accurately characterize the tunnel EDZ, and the SRM method may be a good option to characterize the EDZ in complex geo-environments.

The mechanical behavior in the EDZ area is further examined using the monitored stresses and strains in the measurement spheres. The data of the large sphere correspond to global changes of the model, where the stresses monitored are suggested to be the same as the far-field stresses applied to the model. While, the data from the smaller spheres of 1–4 (Fig. 6c), as each only reflecting a small domain in the rock mass, correspond to the localized changes of stress and strain. This kind of information is useful to explain the failure mechanism of the rock mass at the meso-scale. Figure 8a–c show the stress-strain relationships in the three directions,
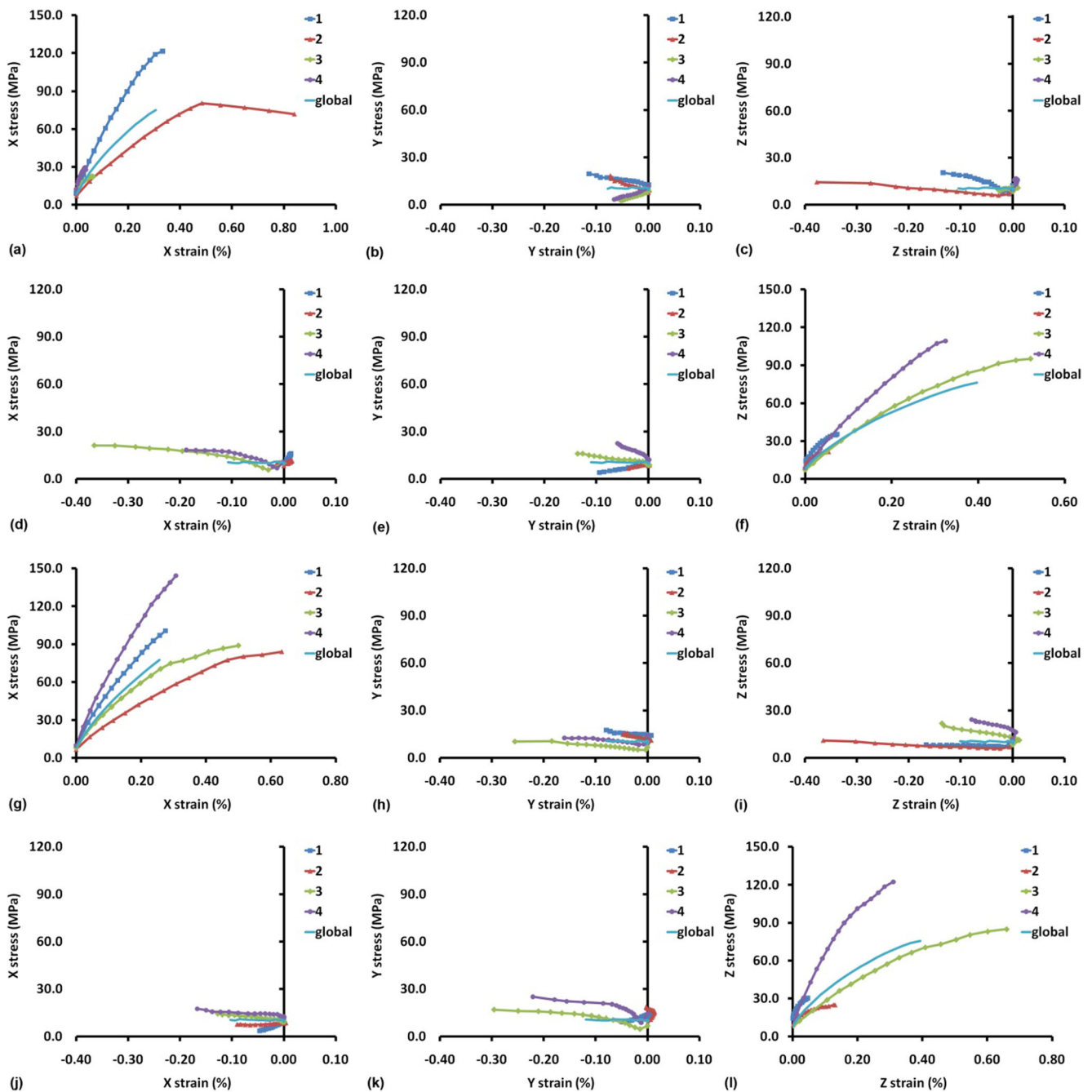
Fig. 8 Stress-strain relationships monitored from the global sphere and localized spheres of 1–4: **a**–**c** tunnel in the Y direction, $\sigma_x = 75.0$ MPa; **d**–**f** tunnel in the Y direction, $\sigma_z = 75.0$ MPa; **g**–**i** tunnel in the X direction, $\sigma_x = 75.0$ MPa; **j**–**l** tunnel in the X direction, $\sigma_z = 75.0$ MPa. The dips of the joint sets in the models are 60° and 39°

respectively, corresponding to the model shown in Fig. 7a. Here, compression and tension are denoted by positive and negative values, respectively. For description convenience, the monitored stress is marked by the sphere ID and direction, for instance, σ_{1x} is the X stress monitored by sphere 1 located near the roof, and σ_{3z} is the Z stress monitored by sphere 3 located near the left side wall. For the first model, the stress concentration is clearly captured at spheres 1 and 2 (roof and floor) in the X direction. As the global σ_x being 75.0 MPa, σ_{1x}

reaches 121.0 MPa. This high level of X stress crushes the rock mass on the tunnel roof and forms the notch failure. While the σ_{2x} passes its peak of 80.5 MPa and decreases to 71.9 MPa, implying that the rock mass within sphere 2 fails and currently reaches its residual stage. As the model is predominantly loaded along the X direction, the X stresses applied to spheres 3 and 4 (side walls) are much lower, with the corresponding stresses all below 30.0 MPa. This level of stress is insufficient to induce obvious damages on the side walls

(Fig. 8a). The effects of the tunnel excavation on the stress and strain in the Y direction are limited. The monitored data from spheres 1–4 suggest that localized rock masses all deform in tension (negative strains). The Y stresses at spheres 1 and 2 increase slightly due to the compression in the X direction, and the Y stresses at spheres 3 and 4 decrease slightly as the X stresses are much lower due to the free boundaries created by the excavation (Fig. 8b). The stress changes in the Z direction are also less significant in comparison with the X stresses. All Z stresses fluctuate towards the confining stress of 10.0 MPa. Noticeably, the strain in the Z direction at sphere 2 is much higher than the strains monitored at other spheres (Fig. 8c). The localized rock mass integrity is essentially destroyed; therefore, the rock matrix is easier to dilate towards the positive Z direction at that sphere, as shown in Fig. 7a.

Figure 8d–f show the changes of stress and strain for the model shown in Fig. 7b, where the tunnel model is the same except the loading condition is in the Z direction. As expected, the changes in the X and Y stresses are less significant behaving as the confining stresses. The X strains at spheres 3 and 4 are higher than the strains elsewhere (Fig. 8d), implying that the deformation near the side walls is higher than the deformation on the roof and floor when the tunnel is axially loaded. While the stresses and strains in the Y direction are limited due to the confining effects (Fig. 8e), the stresses and strains in the Z direction are much higher than other monitored data. For instance, the σ_{3z} and σ_{4z} increase to 95.1 MPa and 109.0 MPa when the global σ_z reaches its designated 75.0 MPa (Fig. 8f). This is again a reflection of stress concentration at spheres 3 and 4. The Z stresses near the tunnel roof and floor are much lower than the stresses monitored near the side walls, and no obvious damages are observed in these locations.

Figure 8g–i display the stresses against strains for the model shown in Fig. 7c, where the tunnel is along the X direction and loaded in the same X direction. Monitoring data from the four localized spheres suggest that stress concentration occurs near all tunnel boundaries, including the roof, floor, and side walls, differing from the other models where the EDZ is mainly observed either near the side walls or the roof and floor. The rock mass at spheres 2 and 3 is weaker in comparison with the rock mass at spheres 1 and 4. The σ_{2x} and σ_{3x} almost reach the peak values, as 84.0 MPa and 88.9 MPa when the global σ_x reaches 75.0 MPa, while the σ_{1x} and σ_{4x} are expected to keep increasing if the model is further loaded in the X direction (Fig. 8g). This conclusion is consistent with the tunnel model shown in Fig. 7c, where the EDZ is localized near the floor (sphere 2) and the left side wall (sphere 3). The rock mass deformation in the Y direction at spheres 3 and 4 are at a higher level as the localized rock masses are free to dilate towards the free tunnel space (Fig. 8h). While in the Z direction, the rock mass at sphere 2 has the largest deformation. Most likely the localized rock mass is broken into pieces and squeezed to the tunnel excavation upward (Fig. 8i).

Figure 8j–l finally show the changes of stress and strain for the model shown in Fig. 7d, the same model shown in Fig. 7c except being loaded in the Z direction. Similarly, the stresses and strains are constrained in the X direction along the tunnel axis (Fig. 8j); the Y strains near the side walls are higher than the Y strains monitored elsewhere, implying a higher level of horizontal deformation along the Y direction (Fig. 8k). In the Z direction, the stress concentration results in higher stresses at spheres 3 and 4 (Fig. 8l). The slope of the stress-strain curve monitored at sphere 3 is lower than the slope of the curve from sphere 4. The rock mass modulus at sphere 3 is therefore lower than the rock mass modulus at sphere 4, implying that the rock mass failure involves more structure-controlled mechanical behavior. This may explain the localization of the tunnel EDZ near the right side wall where sphere 4 is placed.

Effects of joint orientation on the tunnel EDZ

Despite previous tunnel EDZ models, four additional models are constructed and examined, as shown in Fig. 9. The joints in the models are rotated to be horizontally and vertically distributed, similar to the models constructed for the rock mass characterization. The models are confined and loaded exactly the same as the previous EDZ models. In this manner, the effects of joint orientation on the tunnel EDZ can be compared and thoroughly characterized. In general, the area of the tunnel EDZ is reduced when the loading stress reaches 75.0 MPa, in comparison with the EDZ models where inclined joints are simulated. This is attributed to the higher rock mass strength controlled by the rotated joints. As previously verified, the rock mass is strengthened when this type of joint distribution is simulated in the model. The rock mass damages are observed near the roof and floor when the model is subjected to squeezing in the X direction. Nevertheless, the cracks and existing joints form no continuous damage zone, and this level of rock mass damage is insufficient to induce the EDZ which requires systematic supporting, as shown in Fig. 9a. The tunnel EDZ is observed near the side walls when the same model is loaded in the Z direction; however, the depth of the EDZ is reduced in comparison with the model shown in Fig. 7b. The EDZ depth on the left and right side walls is roughly measured as 1.2 r and 0.6 r, as shown in Fig. 9b. The rock mass damages are also observed when the tunnel is in the X direction and loaded in the same direction; nevertheless, the rock mass damages are once again at a low level and no obvious tunnel EDZ is characterized, as shown in Fig. 9c. The cracks formed between joints are significantly reduced in comparison with the model shown in Fig. 7c. The tunnel EDZ is simulated in the last model with horizontal and vertical joints on the right side wall, with the depth roughly as 0.8 r (Fig. 9d). This depth is still smaller than the EDZ depth simulated in Fig. 7d, as 1.0 r. The two values are comparable but it may not change the fact that the area of the tunnel EDZ is

Fig. 9 Localized tunnel EDZ models: **a** tunnel in the Y direction, $\sigma_x = 75.0$ MPa; **b** tunnel in the Y direction, $\sigma_z = 75.0$ MPa; **c** tunnel in the X direction, $\sigma_x = 75.0$ MPa; **d** tunnel in the X direction, $\sigma_z = 75.0$ MPa. The confining stresses are 10.0 MPa in each model. The dips of the joint sets in the models are 90° and 0°. The disks and dots denote initial joints and secondary cracks when the SRM models are subjected to external loading

(a)   (b)

(c)   2m   (d)
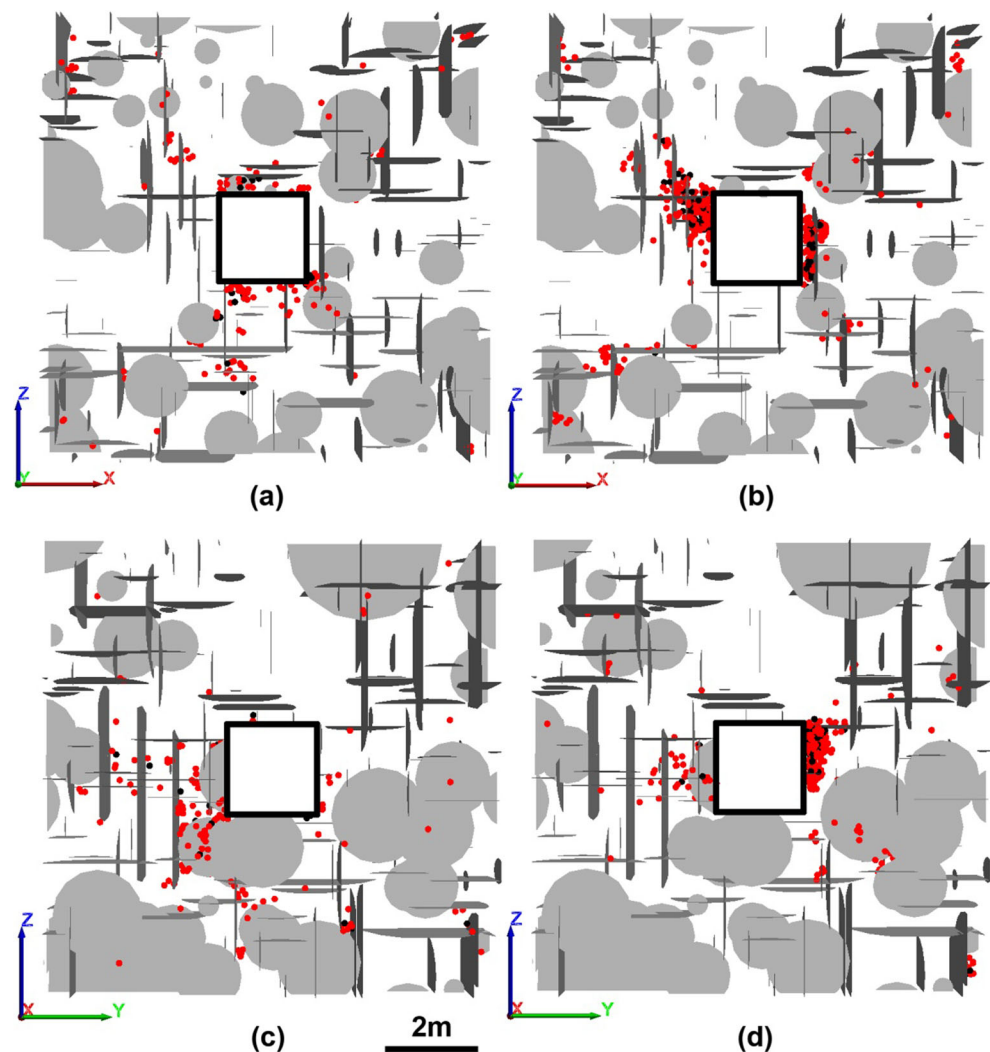
either negligible or significantly reduced when the horizontal and vertical joints are simulated in the models.

Figure 10 shows the relationships of stress and strain monitored at the global and localized measurement spheres of the four additional models. In general, the tendencies of the stress-strain plots are similar to the stress-strain plots derived from the former models with inclined joints. The stress concentration is observed near the tunnel roof and floor when the model is loaded along the X direction. While, the rock mass is squeezed and stress concentration occurs near the side walls when the model is loaded in the vertical direction. In comparison with the previous plots shown in Fig. 8, the stress-strain plots are steeper at the localized rock masses of the stress concentration, typically shown in Fig. 10a–l. Note also that most localized rock masses being squeezed have not yet reached the strength peaks. Meanwhile, the rock mass deformation is limited when the horizontal and vertical joints are simulated. For instance, the highest Z strain is about -0.09% when the tunnel is in the Y direction and squeezed in the X

direction (Fig. 10c), while the highest Z strain increases to -0.38% for the same model only with inclined joints (Fig. 8c). The rock mass deformation is controlled by the deformation of the intact rocks when the horizontal and vertical joints are simulated in the models.

Conclusions

A synthetic rock mass numerical model is applied for characterizations of the rock mass and tunnel EDZ in this research. The block volume is used as a bridge between the DFN models and the descriptive rating towards rock mass structure during GSI characterization. The strength and modulus are compared between the SRM and the GSI/Hoek-Brown system. Numerical models suggest that the SRM method and the GSI/Hoek-Brown system converge well when the joints simulated in the rock mass are inclined and favorable to shear sliding. The numerical strength is higher when the joints are
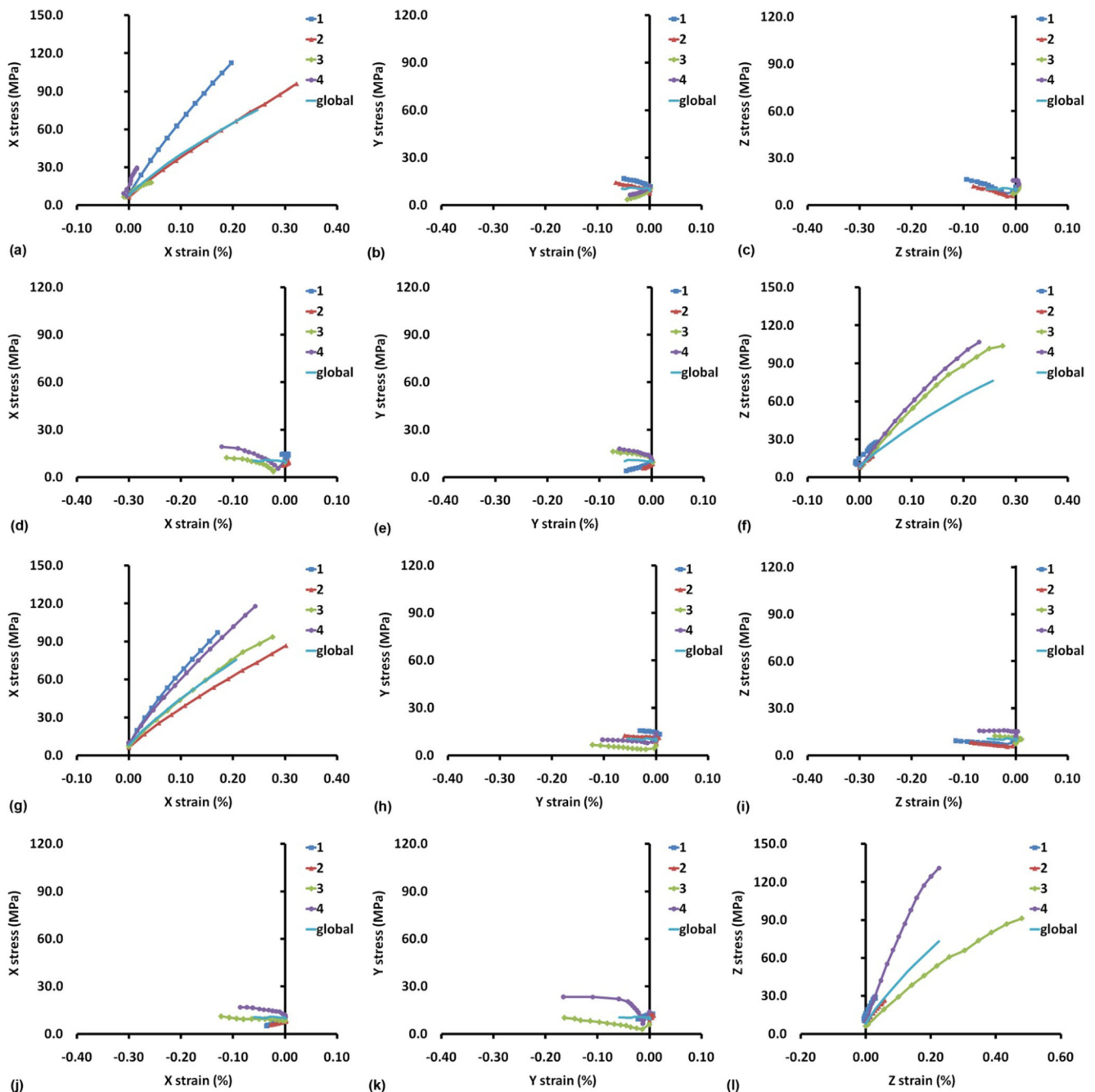
Fig. 10 Stress-strain relationships monitored from the global sphere and localized spheres of 1–4: **a**–**c** tunnel in the Y direction, $\sigma_x = 75.0$ MPa; **d**–**f** tunnel in the Y direction, $\sigma_z = 75.0$ MPa; **g**–**i** tunnel in the X direction, $\sigma_x = 75.0$ MPa; **j**–**l** tunnel in the X direction, $\sigma_z = 75.0$ MPa. The dips of the joint sets in the models are 90° and 0°

horizontally and vertically distributed. In this case, the rock mass failure depends predominantly on intact rock properties, and the empirical GSI/Hoek-Brown system should be applied with care. The SRM method is then used for tunnel EDZ characterization when the rock mass is in varied environments of in situ stresses. Typical notch failures are simulated in one of the SRM models, and more types of the tunnel EDZ are simulated with changed directions of the tunnel and stresses. The tunnel EDZ is essentially a function of the tunnel

orientation, discontinuities within the rock mass, and characteristics of the initial stresses. Monitoring stresses and strains at the localized measurement spheres show detailed mechanical behavior near the tunnel. Stress concentrations are simulated in the rock masses being squeezed. The rock mass deforms towards the free space of the tunnel excavation, behaving as high strains. The area of the tunnel EDZ is significantly reduced when the rock mass is strengthened by the horizontal and vertical joints.

References

Bahaaddini M, Sharrock G, Hebblewhite BK (2013) Numerical investigation of the effect of joint geometrical parameters on the mechanical properties of a non-persistent jointed rock mass under uniaxial compression. Comput Geotech 49:206–225

Bahrani N, Kaiser PK (2016) Numerical investigations of the influence of specimen size on the unconfined strength of defected rocks. Comput Geotech 77:56–67

Cai M, Kaiser PK, Uno H, Tasaka Y, Minami M (2004) Estimation of rock mass deformation modulus and strength of jointed hard rock masses using the GSI system. Int. J. Rock Mech Min Sci 41:3–19

Esmaieli K, Hadjigeorgiou J, Grenon M (2010) Estimating geometrical and mechanical REV based on synthetic rock mass models at Brunswick Mine. Int J Rock Mech Min Sci 47:915–926

Gong FQ, Wu WX, Li TB (2020) Simulation test of spalling failure of surrounding rock min rectangular tunnels with different height-to-width ratios. Bull Eng Geol Environ. https://doi.org/10.1007/s10064-020-01734-w

Hoek E, Diederichs MS (2006) Empirical estimation of rock mass modulus. Int J Rock Mech Min Sci 43:203–215

Hoek E, Carter TG, Diederichs MS (2013) Quantification of the geological strength index chart. ProceedingsProceedings, 47th US Rock Mechanics, 47th US Rock Mechanics/Geomechanics Symposium. ARMA, San Francisco, pp 13–672

Itasca (2012) Particle flow code in 3D (PFC3D), Version 4.0.182, Minnesota, USA

Lei QH, Latham J, Xiang JS, Tsanvg CF (2017) Role of natural fractures in damage evolution around tunnel excavation in fractured rocks. Eng Geol 231:100–113

Marinos V (2019) A revised, geotechnical classification GSI system for tectonically disturbed heterogeneous rock masses, such as flysch. Bull Eng Geol Environ 78:899–912

Martin CD, Christiansson R (2009) Estimating the potential for spalling around a deep nuclear waste repository in crystalline rock. Int J Rock Mech Min Sci 46:219–228

Mas Ivars D, Pierce M, Darcel C, Reyes-Montes J, Potyondy D, Young RP, Cundall PA (2011) The synthetic rock mass approach for jointed rock mass modelling. Int J Rock Mech Min Sci 48:219–244

Mehranpour MH, Kulatilake P, Ma XG, He MC (2018) Development of new three-dimensional rock mass strength criteria. Rock Mech Rock Eng 51:3537–3561

Palmstrom A (2005) Measurements of and correlation between block size and rock quality designation (RQD). Tunn Undergr Space Tech 20:362–377

Perras M, Wannenmacher H, Diederichs MS (2015) Underground excavation behaviour of the Queenston Formation: tunnel back analysis for application to shaft damage dimension prediction. Rock Mech Rock Eng 48:1647–1671

Poulson BA, Adhikary DP, Elmouttie MK, Wilkins A (2015) Convergence of synthetic rock mass modelling and the Hoek-Brown strength criterion. Int J Rock Mech Min Sci 80:171–180

Rogers S, Elmo D, Webb G, Catalan A (2015) Volumetric fracture intensity measurement for improved rock mass characterization and fragmentation assessment in block caving operations. Rock Mech Rock Eng 48:633–649

Song YH, Xue HS, Ju GH (2020) Comparison of different approaches and development of improved formulas for estimating GSI. Bull Eng Geol Environ. https://doi.org/10.1007/s10064-020-01739-5

Vallejos JA, Suzuki K, Brzovic A, Mas Ivars D (2016) Application of synthetic rock mass modeling to veined core-size samples. Int J Rock Mech Min Sci 80:171–180

Wang YC, Jing HW, Su HJ, Xie JY (2017a) Effect of a fault fracture zone on the stability of tunnel-surrounding rock. Int J Geomech 17:1–20

Wang YC, Jing HW, Yu LY, Su HJ, Luo N (2017b) Set pair analysis for risk assessment of water inrush in karst tunnels. Bull Eng Geol Environ 76:1199–1207

Wang YC, Geng F, Yang SQ, Jing HW, Meng B (2019) Numerical simulation of particle migration from crushed sandstones during groundwater inrush. J Hazar Mat 362:327–335

Yang HQ, Huang D, Yang XM, Zhou XP (2013) Analysis model for the excavation damage zone in surrounding rock mass of circular tunnel. Tunn Undergr Space Tech 35:78–88

Yang WD, Zhang QB, Ranjith PG (2019) A damage mechanical model applied to analysis of mechanical properties of jointed rock masses. Tunn Undergr Space Tech 84:113–128

Zhang XP, Wong LNY (2012) Cracking processes in rock-like material containing a single flaw under uniaxial compression: a numerical study based on parallel bonded-particle model approach. Rock Mech Rock Eng 45:711–737

Zhang Y, Stead D, Elmo D (2015) Characterization of strength and damage of hard rock pillars using a synthetic rock mass method. Comput Geotech 65:56–72

Zhang QB, He L, Zhu WS (2016) Displacement measurement techniques and numerical verification in 3D geomechanical model tests of an underground cavern group. Tunn Undergr Space Tech 56:54–64